ESAIM: PROCEEDINGS, June 2008, Vol. 23, p. 98-113
L. Boudin, C. Grandmont, Y. Maday, B. Maury, B. Sapoval & J.-F. Gerbeau, Editors

TOWARDS STRESSES AND STRAINS IN THE RESPIRATORY SYSTEM

Lena Wiechert[1], Timon Rabczuk[1,2], Andrew Comerford[1], Robert Metzke[1] and Wolfgang A. Wall[1]

Abstract. This paper is concerned with coupled problems in the human respiratory system with emphasis on mechanical ventilation. We focus on the modeling aspects of pulmonary alveoli and the lower airways against the background of acute lung diseases. In this connection occurring stresses and strains are of substantial interest.

For the first generations of the bronchial tree, a geometry based on human computer tomography scans obtained from in-vivo experiments is employed. The deformability of airway walls is taken into account to study airflow structures and airway wall stresses for a number of different scenarios. Therefore we carried out fluid-structure interaction (FSI) simulations under transient incompressible flow conditions. Both models for healthy and diseased lungs are studied under normal breathing as well as under mechanical ventilation.

Our alveolar model is based on three-dimensional artificial random geometries generated with the help of a new labyrinthine algorithm ensuring preservation of overall minimal mean pathlength. A polyconvex hyperelastic material model incorporating general histologic information is employed to realistically describe alveolar parenchymal tissue properties. The influence of surface-active agents (the so-called surfactant) on the overall mechanical behavior of pulmonary alveoli is investigated. For this purpose an adsorption-limited model relating surface stresses to the interfacial concentration of surfactant is used.

Introduction

Mechanical ventilation of the human lung plays a significant role in medicine, especially in case of patients with acute lung diseases such as ALI (acute lung injury) and ARDS (acute respiratory distress syndrome) where it is known to be a vital supportive therapy. Improper methods of ventilation, however, can cause mechanical overstraining of parenchymal tissue resulting in additional inflammatory injuries. This complication is commonly called ventilator-induced lung injury (VILI) and is responsible for a significant increase in mortality rate.

Since up to now it is unclear how to improve ventilation strategies in order to prevent VILI and thereby minimize mortality, we want to bring a little more light into some of the involved phenomena.

In the following, we will focus on the numerical modeling of the respiratory system. VILI mainly occurs in the respiratory zone of the lung, thus a detailed alveolar model is developed. Since it is computationally not feasible to study the entire pulmonary system from the trachea down to the alveoli, investigations are restricted

[1] Chair of Computational Mechanics, Technical University of Munich, Boltzmannstraße 15, D-85747 Garching, Germany, {wiechert,comerford,metzke,wall}@lnm.mw.tum.de

[2] Mechanical Engineering Department, University of Canterbury, Private Bag 4800, Christchurch 8140, New Zealand, timon.rabczuk@canterbury.ac.nz

Article published by EDP Sciences and available at http://www.edpsciences.org/proc or http://dx.doi.org/10.1051/proc:082307

to parts of it. Our idea is to establish a realistic 3-dimensional model of a part of the bronchial tree which is linked to the alveoli by means of simplified models representing the unresolved parts of the lung. Since the coupling of the models is still under development, we will present the separate models of lower airways and alveoli in this paper.

The work described here was done on the basis of the research finite element program BACI covering a wide range of applications in computational mechanics, like e.g. multi-field and multi-scale problems, structural and fluid dynamics, material modeling and finite element technology.

The reminder of this paper is organized as follows.

The second chapter deals with fluid-structure interaction (FSI) simulations of unsteady incompressible airflow in an airway model of the first four generations based on computer tomography (CT) scans. After a short overview on the governing equations, our computational models and solution techniques, we present the results of our studies regarding models of healthy and diseased lungs under normal breathing and mechanical ventilation.

In the subsequent chapter we introduce our model of pulmonary alveoli. A novel approach of generating artificial random geometries is presented along with a constitutive model accounting for realistic soft tissue behavior. The incorporation of surface stresses due to surfactant into the alveolar model enables the investigation of interfacial phenomena in the lungs.

Finally, the paper closes with a short summary and outlook to our future work.

1. Fluid Flow in the Lower Airways

We are interested in airflow structures and stress distributions in airway walls of mechanically ventilated patients, particularly those with acute lung diseases as ALI or ARDS. The exposure of the studied parts of the bronchial tree as well as the effect of airflow on lower unresolved parts of the lung – e.g. the respiratory zone – are of increasing importance when investigating VILI phenomena.

Most existing numerical analyses in the respiratory system were performed with idealized geometries such as the Weibel- [1] or Horsfield- [2] models. We have found severe differences in flow characteristics between artificial and real geometries of the bronchial tree. We compared airflow patterns in planar and non-planar Weibel geometries with an azimuthal angle of 90 degrees to those obtained for a CT geometry. We found that airflow structures were significantly different for the studied cases. Secondary airflow intensities were higher in the CT geometry compared to the Weibel models as illustrated in Figs. 1 and 2. In this paper we therefore investigate flow in a CT-based geometry of the first four generations of lower airways. The CT scans are obtained from in-vivo experiments of patients under normal breathing and mechanical ventilation.

Remarkably, almost all existing studies disregard the influence of airway wall flexibility on flow structures. In this study we try to get a first insight in fluid-structure interaction effects in the first generations of the bronchial

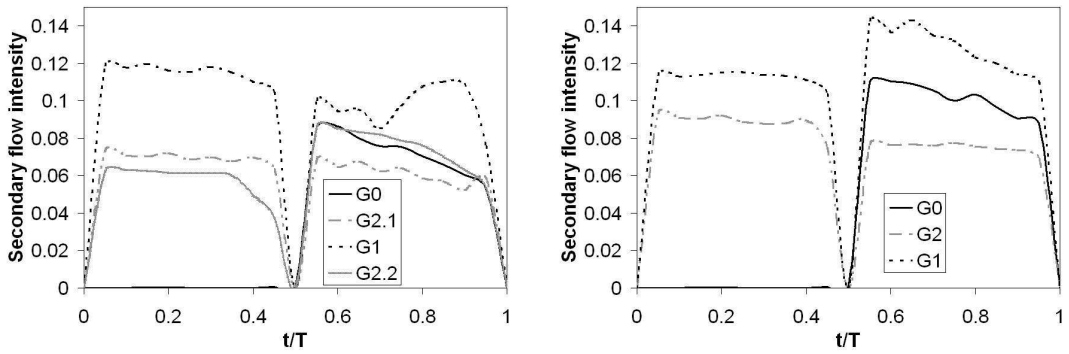

Figure 1. Secondary airflow intensities in the inplane (left) and offplane (right) Weibel model. Tubes are numbered in ascending order starting with the trachea

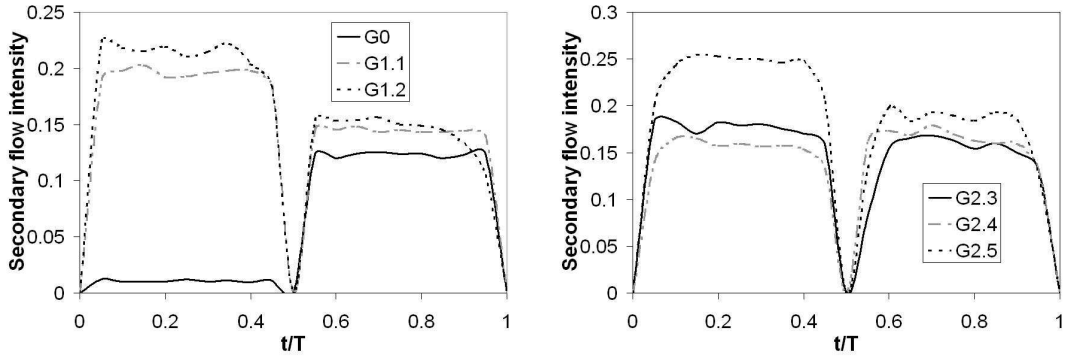

FIGURE 2. Secondary airflow intensities in the CT scan based geometry. Tubes are numbered in ascending order starting with the trachea

tree. Despite the fact that the employed boundary conditions are initially sometimes non-physiological, the adopted model will help understanding some involved phenomena in VILI.

1.1. Governing Equations

We assume an incompressible Newtonian fluid under laminar and transient flow conditions. The underlying governing equation is the Navier Stokes equation formulated on time dependent domains.

$$\left.\frac{\partial \boldsymbol{u}}{\partial t}\right|_{\boldsymbol{\chi}} + \left(\boldsymbol{u} - \boldsymbol{u}^G\right) \cdot \boldsymbol{\nabla}\boldsymbol{u} - 2\nu\boldsymbol{\nabla} \cdot \boldsymbol{\varepsilon}(\boldsymbol{u}) + \nabla p = \boldsymbol{f}^F \qquad \text{in } \Omega^{\mathrm{F}} \tag{1}$$

$$\boldsymbol{\nabla} \cdot \boldsymbol{u} = 0 \qquad \text{in } \Omega^{\mathrm{F}} \tag{2}$$

where $\mathbf{u}$ is the velocity vector, $\mathbf{u}^G$ is the grid velocity vector, p is the pressure and $\mathbf{f}^F$ is the body force vector. A superimposed F refers to the fluid domain and $\boldsymbol{\nabla}$ denotes the nabla operator. The parameter $\nu = \mu/\rho^F$ is the kinematic viscosity with viscosity μ and fluid density ρ^F. The kinematic pressure is represented by p where $\bar{p} = p\,\rho^F$ is the physical pressure within the fluid field. The balance of linear momentum (1) refers to a deforming arbitrary Lagrangean Eulerian (ALE) frame of reference denoted by $\boldsymbol{\chi}$ where the geometrical location of a mesh point is obtained from the unique mapping $\mathbf{x} = \varphi(\boldsymbol{\chi}, t)$, cf. e.g. [3].

The stress tensor of a Newtonian fluid is given by

$$\boldsymbol{\sigma}^F = -\bar{p}\,\boldsymbol{I} + 2\mu\boldsymbol{\varepsilon}(\boldsymbol{u}) \tag{3}$$

with the compatibility condition

$$\boldsymbol{\varepsilon}(\boldsymbol{u}) = \frac{1}{2}\left(\boldsymbol{\nabla}\boldsymbol{u} + \boldsymbol{\nabla}\boldsymbol{u}^T\right) \tag{4}$$

where $\boldsymbol{\varepsilon}$ is the rate of deformation tensor. The initial and boundary conditions are

$$\begin{aligned} \boldsymbol{u}(t=0) &= \boldsymbol{u}_0 && \text{in } \Omega^{\mathrm{F}} \\ \boldsymbol{u} &= \hat{\boldsymbol{u}} && \text{on } \Gamma^{\mathrm{F}}_{\mathrm{D}} \\ \boldsymbol{\sigma} \cdot \boldsymbol{n} &= \hat{\boldsymbol{h}}^F && \text{on } \Gamma^{\mathrm{F}}_{\mathrm{N}} \end{aligned} \tag{5}$$

where $\Gamma^{\mathrm{F}}_{\mathrm{D}}$ and $\Gamma^{\mathrm{F}}_{\mathrm{N}}$ denote the Dirichlet and Neumann partition of the fluid boundary, respectively, with normal $\boldsymbol{n}$, with $\Gamma^{\mathrm{F}}_{\mathrm{D}} \bigcap \Gamma^{\mathrm{F}}_{\mathrm{N}} = \emptyset$. $\hat{\boldsymbol{u}}$ and $\hat{\boldsymbol{h}}^F$ are the prescribed velocities and tractions.

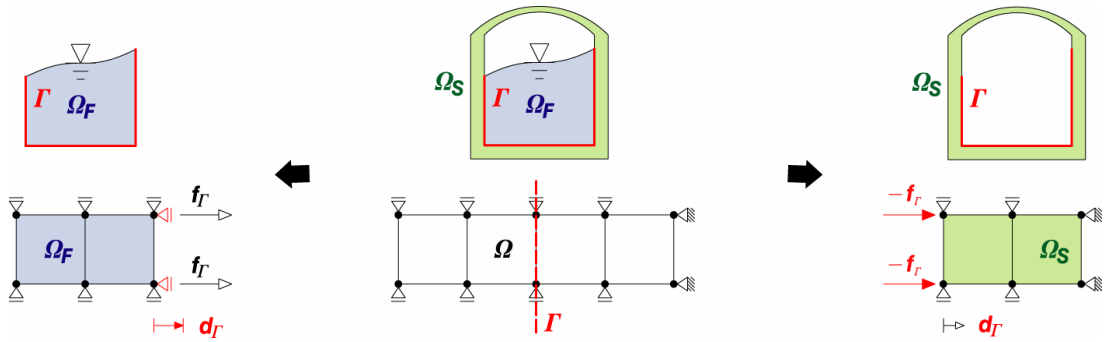

FIGURE 3. FSI coupling: the domain is decomposed into a fluid part Ω_F and a solid part Ω_S with a common interface Γ where displacement and traction continuity has to be fulfilled

The governing nonlinear equation in the solid domain is the linear momentum equation given by

$$\rho^S \ddot{\boldsymbol{d}} = \boldsymbol{\nabla}_0 \cdot (\boldsymbol{F} \cdot \boldsymbol{S}) + \rho^S \boldsymbol{f}^S \qquad \text{in } \Omega^{\mathrm{S}} \tag{6}$$

where $\boldsymbol{d}$ are the displacements, $\boldsymbol{S}$ is the second Piola-Kirchhoff stress tensor and $\boldsymbol{F}$ is the deformation gradient. Superimposed dots denote material time derivatives and the superimposed S refers to the solid domain. ρ^S and $\boldsymbol{f}^S$ represent the density and body force, respectively.

The initial and boundary conditions are

$$\begin{aligned} \boldsymbol{d}(t=0) &= \boldsymbol{d}_0 && \text{in } \Omega^{\mathrm{S}} \\ \dot{\boldsymbol{d}}(t=0) &= \dot{\boldsymbol{d}}_0 && \text{in } \Omega^{\mathrm{S}} \\ \boldsymbol{d} &= \hat{\boldsymbol{d}} && \text{on } \Gamma^{\mathrm{S}}_{\mathrm{D}} \\ \boldsymbol{S} \cdot \boldsymbol{n} &= \hat{\boldsymbol{h}}^S && \text{on } \Gamma^{\mathrm{S}}_{\mathrm{N}}, \end{aligned} \tag{7}$$

where $\Gamma^{\mathrm{S}}_{\mathrm{D}}$ and $\Gamma^{\mathrm{S}}_{\mathrm{N}}$ denote the Dirichlet and Neumann partition of the structural boundary, respectively, with $\Gamma^{\mathrm{S}}_{\mathrm{D}} \bigcap \Gamma^{\mathrm{S}}_{\mathrm{N}} = \emptyset$. $\hat{\boldsymbol{d}}$ and $\hat{\boldsymbol{h}}^S$ are the prescribed displacements and tractions.

Within this paper, we will account for geometrical nonlinearities but we will assume the material to be linear elastic. Since we expect only small strains and due to lack of experimental data, this assumption seems to be fair for first studies. In line with [4] we assume that human lungs are stress-free under load-free conditions.

1.2. Partitioned Solution Approach for Fluid-Structure Interaction

A partitioned solution approach is used based on a domain decomposition that separates the fluid and the solid, confer also Fig. 3. The "wet" surface of the solid acts hereby as a natural coupling interface Γ across which displacement and traction continuity at all discrete time steps have to be fulfilled:

$$\boldsymbol{d}_\Gamma(t) \cdot \boldsymbol{n} = \boldsymbol{r}_\Gamma(t) \cdot \boldsymbol{n} \qquad \text{and} \qquad \boldsymbol{u}_\Gamma(t) \cdot \boldsymbol{n} = \boldsymbol{u}^G_\Gamma(t) \cdot \boldsymbol{n} = \left. \frac{\partial \boldsymbol{r}_\Gamma(t)}{\partial t} \right|_{\boldsymbol{\chi}} \cdot \boldsymbol{n} \tag{8}$$

$$\boldsymbol{\sigma}^S_\Gamma(t) \cdot \boldsymbol{n} = \boldsymbol{\sigma}^F_\Gamma(t) \cdot \boldsymbol{n} \tag{9}$$

where $\boldsymbol{r}$ are the displacements of the fluid mesh and $\boldsymbol{n}$ is the unit normal on the interface. Satisfying the kinematic continuity leads to mass conservation at Γ, satisfying the dynamic continuity yields conservation of linear momentum, and energy conservation finally requires to simultaneously satisfy both continuity equations.

The coupled problem is solved using a Dirichlet-Neumann partitioning between fluid and structure. Forces generated by fluid pressure and friction are exerted on the structural interface as Neumann boundary conditions,

whereas structural displacements at Γ are transferred into velocities and used as a Dirichlet condition of the fluid. The solution of the problem fulfilling both (8) and (9) is found by means of an iterative approach. The algorithmic framework of the partitioned FSI analysis is discussed in detail elsewhere, cf. e.g. [5], [6], [7], [8], [9], [10] and [11].

1.3. **Computational Model**

In the fluid domain, we use linear tetrahedral elements with GLS stabilization (cf. [12], [13] and [14]). The airways are discretized with 7-parameter triangular shell elements (cf. [15], [16]). We refined the mesh from 110,000 up to 520,000 fluid elements and 50,000 to 295,000 shell elements, respectively, until the calculated mass flow rate was within a tolerance of 1%.

Time integration is done with a one-step-theta method with fixed-point iteration and $\theta = 2/3$. For the fluid, we employ a generalized minimal residual (GMRES) iterative solver with ILU-preconditioning.

We study normal breathing under moderate activity conditions with a tidal volume of $2l$ and a breathing cycle of $4s$, i.e. $2s$ inspiration and $2s$ expiration. Moreover, we consider mechanical ventilation where experimental data from the respirator is available, see Fig. 4.

A pressure-time history can be applied at the outlets such that the desired tidal volume is obtained. For the case of normal breathing, the pressure-time history at the outlets would be sinusoidal, negative at inspiration and positive at expiration as it occurs in "reality". The advantage is that inspiration and expiration can be handled quite naturally within one computation. The difficulty is to calibrate the boundary conditions such that the desired tidal volume is obtained which is an iterative procedure.

To investigate airflow in the diseased lung, non-uniform boundary conditions are assumed. For that purpose, we set the pressure outlet boundary conditions consistently twice and three-times higher on the left lobe of the lung as compared to the right lobe. This should model a higher stiffness resulting from collapsed or highly damaged parts of lower airway generations as a first approach.

1.4. **Results**

In the following a selection of first results of our investigations is presented based on a number of simplifying assumptions. Refined models better representing the physiological situation are currently under development, confer section 3.

1.4.1. *Normal Breathing – Healthy Lung*

At inspiration the flow in the right bronchus exhibits a skew pattern towards the inner wall, whereas the left main bronchus shows an M-shape, see Fig. 5. The flow pattern is similar in the entire breathing cycle with more or less uniform secondary flow intensities except at the transition from inspiration to expiration. The overall stress distribution at inspiratory peak flow is shown on the left hand side of Fig. 6. Stresses are highest in the

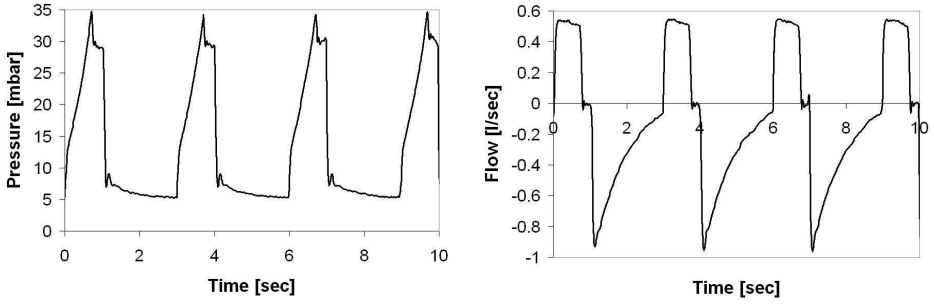

FIGURE 4. Pressure-time and flow-time history of the respirator for the mechanically ventilated lung

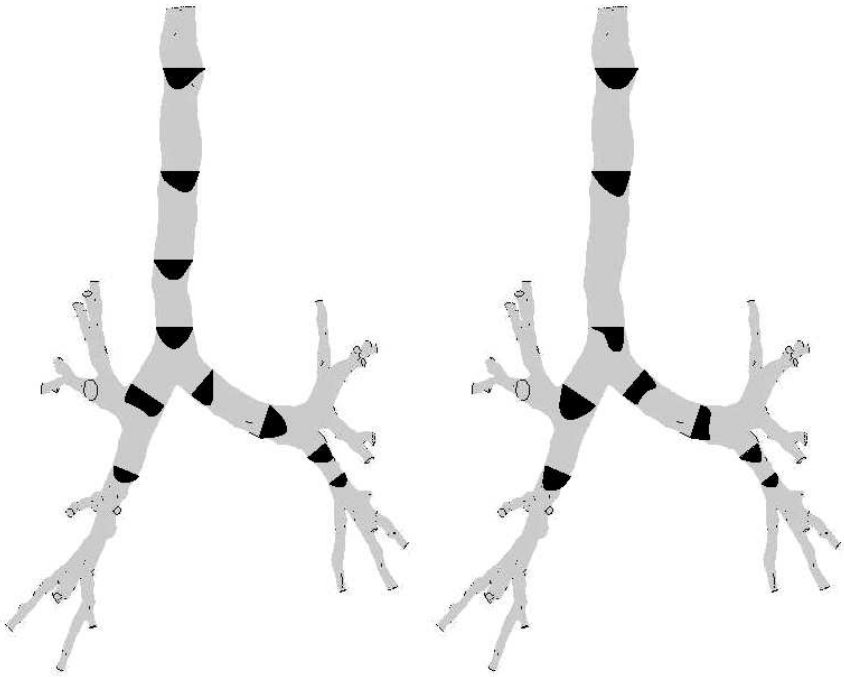

FIGURE 5. Total flow structures at different cross sections for the healthy lung under normal beathing (left) and the diseased lung under mechanical ventilation (right)

trachea as well as at bifurcation points, e.g. the carina. Due to the imposed boundary conditions, velocity and stress distributions as well as normalized mass flow through the outlets are uniform as can be seen in Figs. 6 and 7.

For pure computational fluid dynamics (CFD) simulations differences regarding secondary flow pattern can be observed between FSI and pure CFD simulations (cf. [17]). The largest deviations occur in the fourth generation and range around 17% at selected cross sections.

1.4.2. *Mechanical Ventilation – Healthy Lung*

Airflow patterns under mechanical ventilation quantitatively differ from normal breathing because of the shorter inspiration time, the different pressure-time history curve and the smaller tidal volume. Despite the different breathing patterns, the principal flow structure is qualitatively quite similar in the trachea and the main bronchi. However, flow patterns after generation 2 are different particularly with respect to secondary flow. General airflow characteristics can be seen in Fig. 8 where the distribution of pressure and velocity along with some streamlines are displayed. The stress distribution of the healthy lung under mechanical ventilation is shown in the middle of Fig. 6. Again, due to the imposed boundary conditions, stress distributions as well as normalized mass flow through the outlets are uniform as can also be seen in Fig. 7.

Airflow during expiration differs significantly from inspiratory flow in contrast to normal breathing. At the end of the expiration, the pressure is set almost instantly to the positive endexpiratory pressure (PEEP) value of the ventilator. This results in a high peak flow rate right at the beginning of the expiration, see Fig. 4. The peak flow at this time is more than twice as high as the maximum peak flow rate under inspiration. The flow at the beginning of expiration is unsteady with a significant increase in secondary flow intensity. At the middle of the expiration cycle, airflow becomes quasi-steady and stresses in the airway walls as well as secondary flow intensities decrease again. The bulk of the inspirated tidal air volume is already expirated at that time.

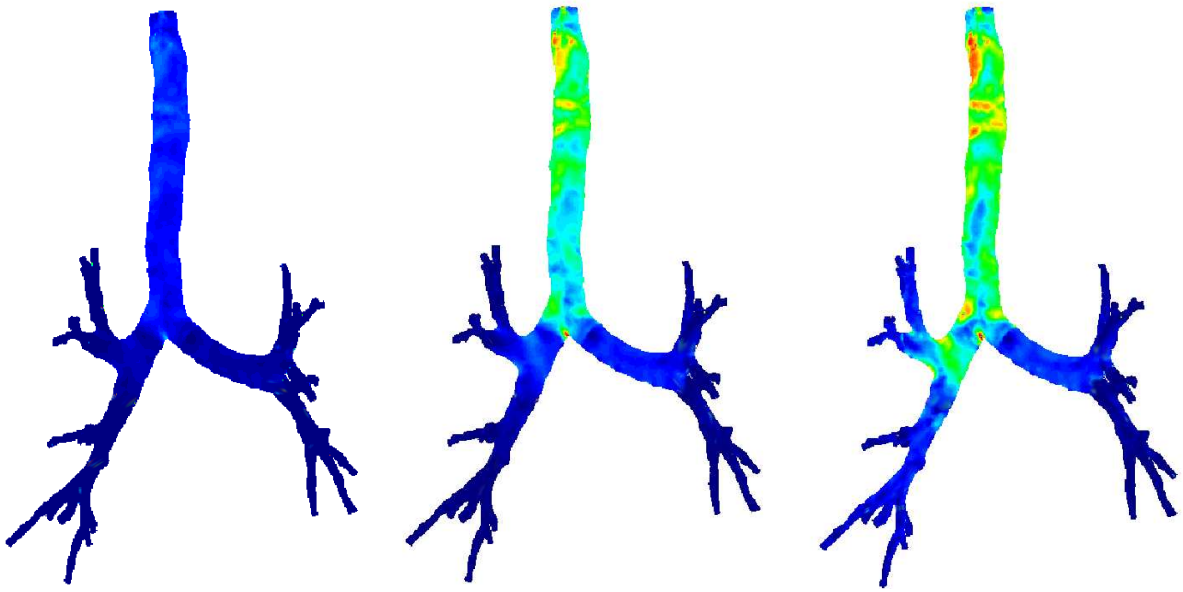

FIGURE 6. Principal tensile stress distribution at inspiratory peak flow rate in the airways of the healthy lung under normal breathing (left) and mechanical ventilation (middle) and in the diseased lung under mechanical ventilation (right)

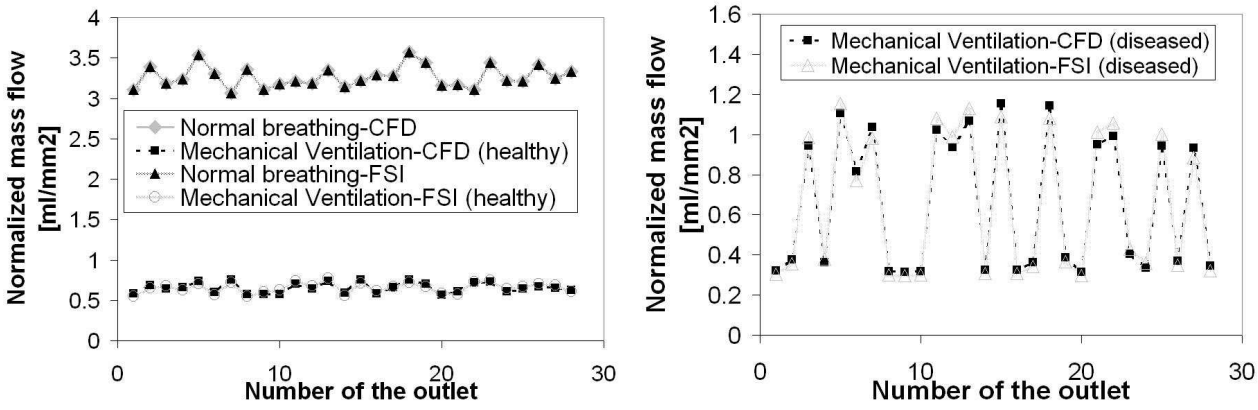

FIGURE 7. Normalized flow distribution at the outlets under normal breathing and mechanical ventilation for the healthy and diseased lung

1.4.3. *Mechanical Ventilation – Diseased Lung*

Airflow structures obtained for diseased lungs differ significantly from those for healthy lungs in inspiration as well as in expiration. Flow and stress distributions are no longer uniform because of the different imposed pressure outlet boundary conditions. Only 30% of the tidal air volume enters the diseased part of the lung, i.e. the left lobe. The normalized mass flow calculated at every outlet of the airway model is shown in Fig. 7.

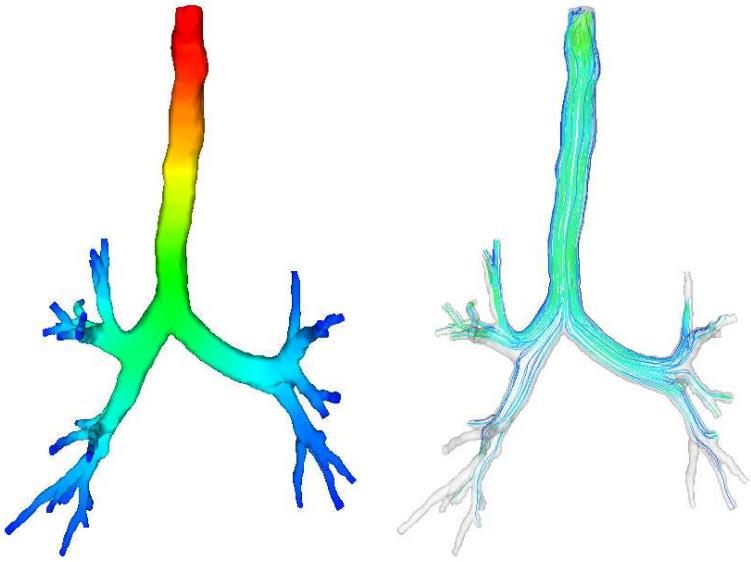

FIGURE 8. Pressure distribution (left) and streamlines (right) for mechanical ventilation of the healthy lung in inspiration. Colors from blue to red indicate increasing pressure and velocity, respectively

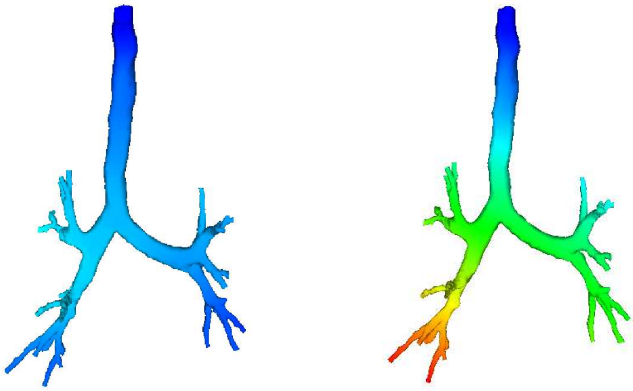

FIGURE 9. Deformation of the healthy (left) compared to the diseased (right) lung. Colors from blue to red indicate increasing absolute displacements

In Fig. 5 the differences in airflow structures of the healthy and diseased lung in terms of discrete velocity profiles during inspiratory flow are visualized.

The secondary flow structures are not only quite different from the healthy lung but they also deviate from the results for diseased lungs obtained in [17] where the airway walls were assumed to be rigid and nonmoving. Thus FSI-forces are significantly larger in simulations of the diseased lung and the influence of airway wall flexibility on the flow should therefore not be neglected. Overall deformations of the bronchial model for the diseased compared to the healthy lung are shown in Fig. 9.

In general airway wall stresses are larger in diseased than in healthy lungs as can be seen in Fig. 6. In the diseased lung stresses are more pronounced in the less ventilated parts due to higher secondary flow intensities

(especially close to the walls) found there. The highest stresses occur at the beginning of expiration. We have modified the expiration curves of the respirator and decreased the pressure less abruptly resulting in a significant reduction of airway wall stresses. This finding is especially interesting with respect to our long-term goal of proposing protective ventilation strategies allowing minimization of VILI.

2. Modeling of Pulmonary Alveoli

VILI mainly occurs at the alveolar level of the lungs in terms of primary mechanical and secondary inflammatory injuries. Primary injuries are consequences of alveolar overexpansion or frequent recruitment and derecruitment inducing high shear stresses. Since mechanical stimulation of cells can result in the release of proinflammatory mediators – a phenomenon commonly called mechanotransduction – secondary inflammatory injuries directly follow and can spread over to other organs resulting in multi-organ failure. According to [18] it is therefore crucial to understand alveolar dynamic behavior in order to investigate mechanisms of VILI.

Subsequently our model of pulmonary alveoli will be presented. Due to the complexity and largeness of involved problems parallel computation and the employment of efficient solvers is sorely needed. More details on related issues can be found in [19].

2.1. **Labyrinthine Algorithm**

Since currently no real geometries of pulmonary alveoli are available for simulations due to too low resolutions of conventional imaging techniques, we are interested in finding ways to artificially generate them with the help of a labyrinthine algorithm as introduced in [20]. This concept is based on the assumption that a minimal mean acinar pathlength is essential in ensuring optimal gas exchange.

In general a labyrinthine algorithm enables the generation of a spatial network of cells by progressively affiliating cells to a given arbitrarily located starting cell following certain connection rules. Point of origin is an a priori defined assemblage of identical space-filling and initially closed base cells. By successively opening faces connections of all cells to the starting cell are established. It is automatically guaranteed that each cell is passed only once except in case of branching cells and detours are precluded.

If a cell is affiliated in the course of the labyrinth creation, it is stored in a queue. In every step, the cell located in front of the queue is set active and thus can create a path to a new cell by randomly choosing one of its neighboring cells that are not already passed. Afterwards, the active cell and the just affiliated new cell are moved to the end of the queue. If, however, the active cell has no unpassed neighbors in the beginning or at the end of the step, it is deleted from the queue. The procedure is repeated until the queue is worn out.

The conventional algorithm is restricted to very simple geometries, i.e. square and cubic cells, hence acinar geometries are locally fairly unrealistic. A more authentic shape for alveolar ducts and alveoli is the so-called tetrakaidecahedron or truncated octahedron. We developed a new variant of the algorithm applicable to tetrakaidecahedral base cells. For these complex geometries also multiple diagonal connections of cells are possible. In order to enforce a minimal mean pathlength it has to be explicitly verified that the pathway to the randomly chosen new cell via the currently active cell is an optimal one. If no shorter pathlength via other cells in the queue exists, then the new cell can be connected to the active cell. Otherwise another possible new cell has to be selected from the range of neighbors. In case that either no other neighboring cell is at hand or no other adjacent cell can be affiliated optimally, the subsequent cell in the queue is set active. The generality of the introduced approach with respect to varying cell numbers or starting points can be shown. Examples of created labyrinthine pathways through alveolar assemblages of different sizes are depicted in Fig. 10. Predicted mean longitudinal pathlength compares well with experimental data obtained from rubber silicone casts of human lungs.

An example of a corresponding geometry of alveolar ensembles can be found in Fig. 11, where a calculated displacement distribution for an assemblage of 91 alveoli under hydrostatic pressure is shown. For a more detailed presentation we refer to [21].

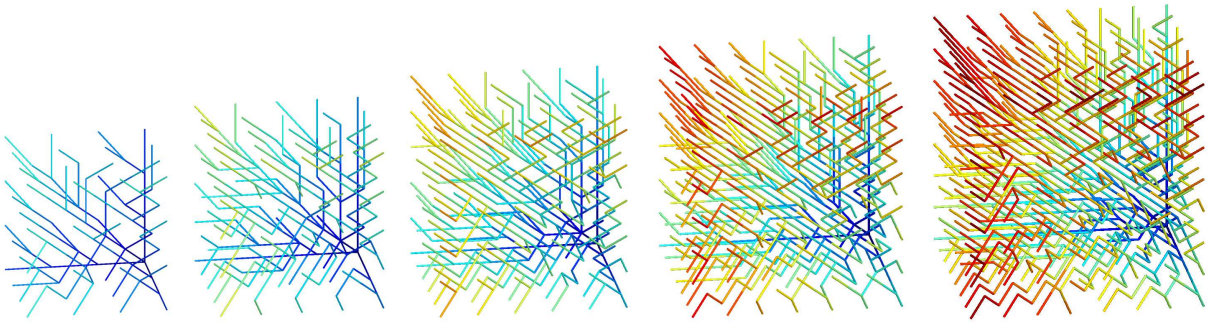

FIGURE 10. Connections of centers of tetrakaidecahedral cells in different alveolar ensembles based on the novel labyrinthine algorithm. Colors characterize the distance to the starting cell

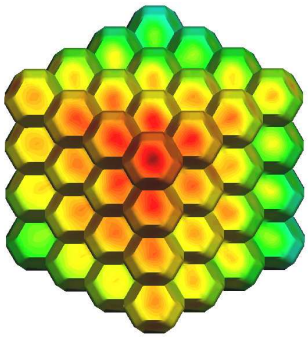

FIGURE 11. Alveolar ensemble under hydrostatic pressure. Connections between alveoli are established with the help of the novel labyrinthine algorithm. Colors from blue to red indicate increasing absolute displacements

2.2. **Organization and Modeling of Alveolar Parenchymal Tissue**

Alveolar tissue is composed of interstitial cells and the so-called extracellular matrix (ECM) consisting of connective tissue fiber networks and an amorphous ground substance made up mainly of proteoglycans. Since the contribution of interstitial cells to parenchymal mechanics seems to be marginal according to [22], we focus on modeling the behavior of the ECM.

Under the assumption of hyperelasticity, we can describe the mechanical behavior of the ECM via a potential, the so-called strain-energy density function W relating the second Piola-Kirchhoff stress tensor $\boldsymbol{S}$ to the right Cauchy-Green strain tensor $\boldsymbol{C}$ as follows

$$\boldsymbol{S} = 2\frac{\partial W}{\partial \boldsymbol{C}}. \tag{10}$$

The strain-energy function used in the following is based on [23], [24] and [25]. W is composed of functions for the matrix including ground substance and elastin fibers and for the collagen fiber families, each fulfilling the principles of objectivity and material symmetry as well as the requirements of polyconvexity and the stress-free reference state.

For the ground substance, a modification of the isotropic neo-Hookean material model is used

$$W_{gs} = c\left(\frac{I_1}{I_3^{\frac{1}{3}}} - 3\right) \qquad c > 0 \tag{11}$$

with c representing a shear-modulus-like parameter and I_1 and I_3 being the first and third invariants of the right Cauchy-Green tensor.

Additionally, a penalty function is employed for the enforcement of incompressibility

$$W_{pen} = \epsilon \left(I_3^{\gamma} + \frac{1}{I_3^{\gamma}} - 2 \right) \qquad \epsilon > 0, \quad \gamma > 1 \tag{12}$$

with ϵ and γ as penalty parameters.

The orientation of the collagen fibers varies according to an orientation density distribution. A general structural tensor $\mathbf{H}$ is introduced

$$\mathbf{H} = \kappa \mathbf{I} + (1 - 3\kappa)\, \mathbf{a} \otimes \mathbf{a} \tag{13}$$

with $\mathbf{a}$ as prescribed fiber direction and κ as a parameter derived from the orientation density distribution function $\rho(\theta)$

$$\kappa = \frac{1}{4} \int_0^{\Pi} \rho(\theta) sin^3(\theta) d\theta. \tag{14}$$

Fiber orientation in alveolar tissue seems to be rather random, hence lung parenchyma can be treated as a homogeneous, isotropic continuum following [26]. In that case κ is equal to $\frac{1}{3}$.
A new invariant K of the right Cauchy-Green tensor is defined by

$$K = \mathrm{tr}\,(\boldsymbol{C}\boldsymbol{H}) \tag{15}$$

where tr(.) denotes the trace of a tensor. The strain-energy function of the non-linear collagen fiber network then reads

$$W_{fib} = \begin{cases} \frac{k_1}{2k_2} \left[exp\left[k_2 \left(K - 1 \right)^2 \right] - 1 \right] & \text{for } K \geq 1 \\ 0 & \text{for } K < 1 \end{cases} \tag{16}$$

with $k_1 \geq 0$ as a stress-like parameter and $k_2 > 0$ as a dimensionless parameter.

Finally, our strain-energy density function takes the following form

$$W = W_{gs} + W_{fib} + W_{pen}. \tag{17}$$

We obtain the corresponding second Piola-Kirchhoff stress tensor and the fourth order constitutive tensor by determining the first and second derivatives of the strain-energy density function $W(\boldsymbol{C})$ with respect to $\boldsymbol{C}$.

Unfortunately only very few experimental data are published regarding the mechanical behavior of alveolar tissue. To the authors' knowledge, no material parameters for single alveolar walls are derivable since up to now only parenchyma was tested (see for example [27], [28], [29]). Therefore we fitted the material model to experimental data published in [30] for lung tissue sheets. Consequently, current parameters model a homogenized continuum of alveolar tissue and air rather than a single alveolar interseptum. The parameters found for ground substance and fiber function are $c = 1kPa$, $k_1 = 13.5kPa$ and $k_2 = 76.5$, the penalty parameters were chosen to be $\epsilon = 10kPa$ and $\gamma = 1.0$.

2.3. **Modeling of Interfacial Phenomena due to Surfactant**

Pulmonary alveoli are covered by a thin, continuous liquid lining with a monomolecular layer of surface active agents (the so-called surfactant) on top of it. It is widely believed that the resulting interfacial phenomena contribute significantly to the lungs' retraction force. That is why taking into account surface stresses appearing in the liquid lining of alveoli is of significant importance.

For our model of pulmonary alveoli we are not primarily interested in the liquid lining itself but rather in its influence on the overall mechanical behavior. Therefore we do not model the aqueous hypophase and the surfactant layer explicitly but consider the resulting surface phenomena in the interfacial structural finite

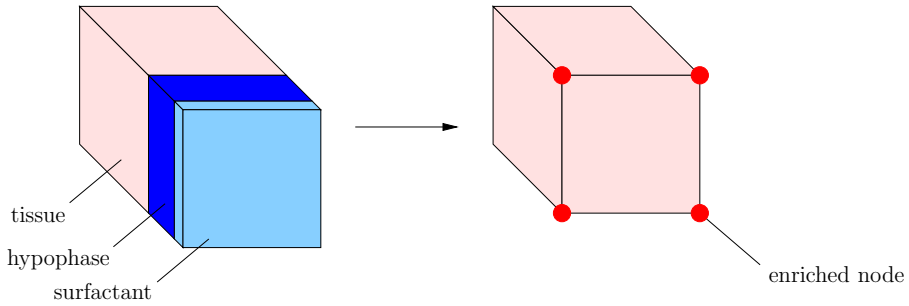

FIGURE 12. Left: Actual configuration. Right: Simplified FE model

element (FE) nodes of the alveolar walls by enriching them with corresponding internal force and tangent stiffness terms (cf. Fig. 12).

The infinitesimal internal work done by the surface stress γ reads

$$dW_{surf} = \gamma(S)\mathrm{d}S \tag{18}$$

with dS being the infinitesimal change in interfacial area. Consequently we obtain for the overall work

$$W_{surf} = \int_{S_0}^{S} \gamma(S^*)\mathrm{d}S^*. \tag{19}$$

The variation of the overall work with respect to the nodal displacements $\mathbf{d}$ then takes the following form

$$\delta W_{surf} = \left(\frac{\partial}{\partial \mathbf{d}} \left(\int_{S_0}^{S} \gamma(S^*)\mathrm{d}S^* \right) \right)^T \delta\mathbf{d} = \left(\frac{\partial}{\partial S} \left(\int_{S_0}^{S} \gamma(S^*)\mathrm{d}S^* \right) \frac{\partial S}{\partial \mathbf{d}} \right)^T \delta\mathbf{d}. \tag{20}$$

Using

$$\frac{\mathrm{d}}{\mathrm{d}x} \int_a^x f(t)\mathrm{d}t = f(x) \tag{21}$$

yields

$$\delta W_{surf} = \gamma(S) \left(\frac{\partial S}{\partial \mathbf{d}} \right)^T \delta\mathbf{d} = \mathbf{f}_{surf}^T \delta\mathbf{d}. \tag{22}$$

with the internal force vector

$$\mathbf{f}_{surf} = \gamma(S) \frac{\partial S}{\partial \mathbf{d}}. \tag{23}$$

The consistent tangent stiffness matrix derived by linearization of (23) therefore reads

$$\mathbf{K}_{surf} = \gamma(S) \frac{\partial}{\partial \mathbf{d}} \left(\frac{\partial S}{\partial \mathbf{d}} \right)^T + \frac{\partial \gamma(S)}{\partial \mathbf{d}} \left(\frac{\partial S}{\partial \mathbf{d}} \right)^T. \tag{24}$$

For details refer also to [31] where, however, an additional surface stress element was introduced in contrast to the above mentioned concept of enriching the interfacial structural nodes.

Unlike e.g. water with its constant surface tension, surfactant exhibits a dynamically varying surface stress γ depending on the interfacial concentration of surfactant molecules. We use the adsorption-limited surfactant model developed in [32] to capture this dynamic behavior.

It is noteworthy that no scaling techniques as in [33], where a single explicit function for γ is used, are necessary, since the employed surfactant model itself delivers the corresponding surface stress depending on both input parameter and dynamic data.

For illustrative purposes, we have plotted the course of γ for different frequencies, amplitudes of area change and model parameters if interfacial area is changed sinusoidally in Figs. 13 and 14.

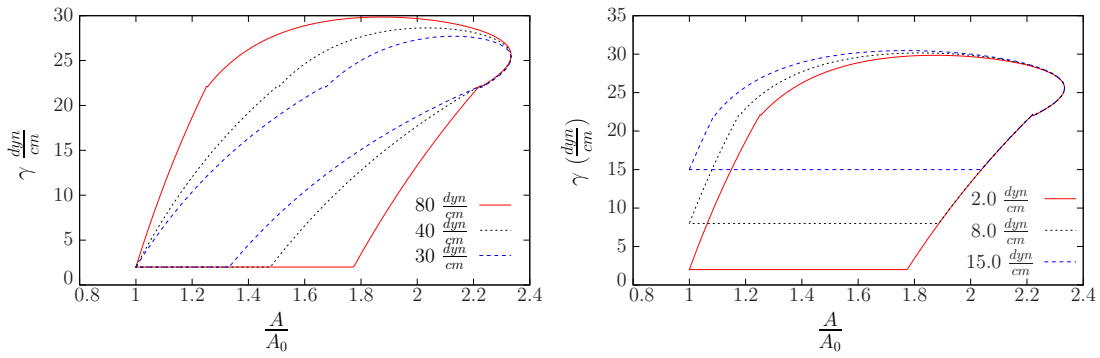

FIGURE 13. Dynamic behavior of surfactant model for different model parameters m_2 and γ_{min} (cf. [32]) known to vary in acute lung diseases

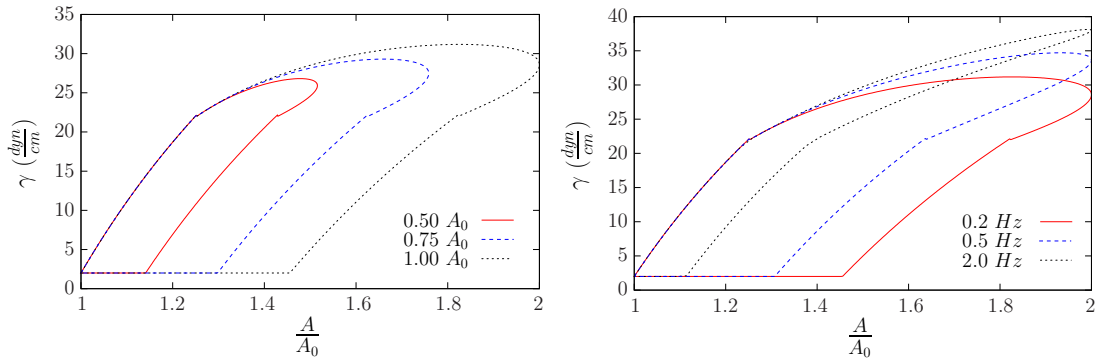

FIGURE 14. Dynamic behavior of surfactant model for different sinusoidal amplitudes and different frequencies

The dynamic surfactant model is particularly advantageous since experimental data for step-wise reconstitution of native surfactant are published in [34] and [35]. Thus with knowledge of the composition of surfactant in diseased states, e.g. in case of ALI/ARDS as reported in [36] and [37], qualitative predictions for the altered behavior of surfactant under cyclic loading are conceivable.

First results of simulations with single alveolar models based on the presented approach of coupling interfacial and structural dynamics are presented in Fig. 15. Clearly, interfacial phenomena play a significant role for the overall mechanical behavior of pulmonary alveoli as can be seen in the differences of overall displacements during sinusoidal hydrostatic loading. The comparison of the results for surfactant and water demonstrates the efficiency of surfactant in decreasing the surface tension of the aqueous hypophase, thereby reducing work of breathing and stabilizing alveoli at low lung volumes. Since interfacial phenomena play a more distinct role for geometries exhibiting a larger curvature, the changes in stiffness are more pronounced for the smaller alveoli shown in the bottom of Fig. 15. Therefore differences between species have to be taken into account when e.g. comparing experimental data.

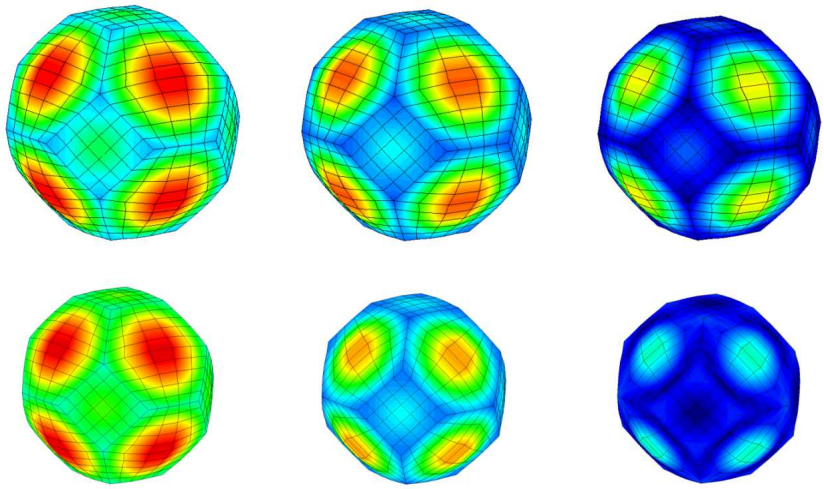

FIGURE 15. Single tetrakaidecahedra loaded by hydrostatic sinusoidally varying pressure on the interior surface. Colors from blue to red indicate increasing absolute displacements under maximum load. From left to right: tissue, tissue covered by surfactant film on the interior surface, tissue covered by water film on the interior surface. Top: Characteristic geometric size comparable to human alveoli. Bottom: Characteristic geometric size comparable to small animals like e.g. hamsters

3. Summary and Outlook

In the present paper, several aspects of modeling the human respiratory system were addressed. The developed approach is not only valuable for analyzing mechanisms of VILI but might also be employed for the prediction of gas exchange and dispersive aerosol transport e.g. in case of inhaled aerosol drugs.

The respiratory system is a highly heterogeneous structure comprising multiple spatial length scales. Since it is neither reasonable nor computationally feasible to simulate the lung on the whole, investigations are restricted to certain interesting parts of it.

Our investigations of airflow and airway wall stresses in the bronchial tree are based on a human CT-scan airway model of the first four generations. For this purpose a partitioned FSI method for incompressible Newtonian fluids under transient flow conditions and geometrically nonlinear structures was applied. We considered normal breathing conditions as well as mechanical ventilation in models of healthy and diseased lungs. Airflow under normal breathing conditions is steady except in the transition from inspiration to expiration. By contrast, airflow under mechanical ventilation is unsteady during the whole breathing cycle due to the given respirator settings. We found that results obtained with FSI and pure CFD simulations are qualitatively similar in case of the healthy lung whereas significant differences can be shown for the diseased lung. Apart from that, stresses are larger in the diseased lung and can be influenced by the choice of ventilation parameters.

The introduced model for pulmonary alveoli comprises the generation of three-dimensional artificial geometries based on tetrakaidecahedral cells. For the sake of ensuring optimal mean pathlength – a feature of great importance regarding effective gas transport in the lungs – a labyrinthine algorithm for complex geometries is employed. A polyconvex hyperelastic material model incorporating general histologic information is applied to describe the behavior of parenchymal lung tissue. Surface stresses stemming from the alveolar liquid lining are considered by enriching interfacial structural nodes of the finite element model. For that purpose, a dynamic adsorption-limited surfactant model is applied. It could be shown that interfacial phenomena influence the overall mechanical behavior of alveoli significantly. Due to different sizes and curvatures of mammalian alveoli, the intensity of this effect is species dependent.

Since currently no reliable material parameters are available for both airway and alveolar tissue, the next step is to perform own experiments. In case of alveolar walls properties will be determined through an inverse analysis taking into account the morphology of the tested tissue sheet as described in [38].

Besides, we currently employ rather non-physiological boundary conditions for both alveolar and airway models. Therefore, only qualitative predictions regarding stresses and flow patterns can be made at present. In order to investigate mechanical ventilation and VILI in particular, the presented models have to be coupled in the future. In fact, the alveolar model can serve as a boundary condition for the airway model and vice versa. First steps concerning this matter are already presented in [39] where the impedance of lower unresolved lung parts is taken into account in airway simulations. Furthermore, we currently develop dynamic multi-scale approaches for modeling coupled problems in the lung, see e.g. [40]. By combining available information on all involved scales, a realistic lung model will be developed that enables the quantitative evaluation of different ventilation strategies with respect to VILI.

Acknowledgement

Support by the German Science Foundation / Deutsche Forschungsgemeinschaft (DFG) is gratefully acknowledged. We also would like to thank our medical partners, i.e. the Guttmann workgroup (J. Guttmann, C. Stahl and K. Möller) at University Hospital Freiburg (Division of Clinical Respiratory Physiology), the Uhlig workgroup (S. Uhlig and C. Martin) at University Hospital Aachen (Institute for Pharmacology and Toxicology) and the Kauczor and Meinzer workgroups (H. Kauczor, M. Puderbach, S. Ley and I. Wegner) at German Cancer Research Center (Division of Radiology / Division of Medical and Biological Informatics).

References

[1] E.R. Weibel. *Morphometry of the human lung*. New York: Academic, 1963.

[2] K. Horsfield, G. Dart, D.E. Olson, G.F. Filley, and G. Cumming. Models of the human bronchial tree. *Journal of Applied Physiology*, 1971.

[3] C. Förster, W.A. Wall, and E. Ramm. On the geometric conservation law in transient flow calculations on deforming domains. *International Journal for Numerical Methods in Fluids*, 50:1369–1379, 2006.

[4] K.O. McKay, B.R. Wiggs, P.D. Pare, and R.D. Kamm. Zero-stress state of intra- and extraparenchymal airways from human, pig, rabbit and sheep lung. *Journal of Applied Physiololgy*, 2002.

[5] C. Förster, W.A. Wall, and E. Ramm. Artificial added mass instabilities in sequential staggered coupling of nonlinear structures and incompressible flows. *Computer Methods in Applied Mechanics and Engineering*, 196:1278–1293, 2007.

[6] U. Küttler and W. A. Wall. Fixed-point fluid-structure interaction solvers with dynamic relaxation. *Comput. Mech.*, DOI:10.1007/s00466-008-0255-5, 2008.

[7] U. Küttler and W. A. Wall. Vector extrapolation for strong coupling fluid-structure interaction solvers. *Applied Mechanics*, 2008, accepted.

[8] W.A. Wall, S. Genkinger, and E. Ramm. A strong coupling partitioned approach for fluid-structure interaction with free surfaces. *Computers and Fluids*, 36:169–183, 2007.

[9] W.A. Wall, A. Gerstenberger, P. Gamnitzer, C. Förster, and E. Ramm. Large deformation fluid-structure interaction – advances in ALE methods and new fixed grid approaches. In H.-J. Bungartz and M. Schäfer, editors, *Fluid-Structure Interaction: Modelling, Simulation, Optimisation*. LNCSE series, Springer, 2006.

[10] W.A. Wall, D.P. Mok, and E. Ramm. Iterative substructuring schemes for fluid structure interaction. In W. Wendland and M. Efendiev, editors, *Analysis and Simulation of Multifield Problems*, pages 349–362. Springer, 2003.

[11] D.P. Mok and W.A. Wall. Partitioned analysis schemes for the transient interaction of incompressible flows and nonlinear flexible structures. In W.A. Wall et al., editor, *Trends in Computational Mechanics*, pages 689–698. CIMNE, Barcelona, Spain, 2001.

[12] V. Gravemeier, W.A. Wall, and E. Ramm. A three-level finite element method for the instationary, incompressible Navier-Stokes equations. *Computer Methods in Applied Mechanics and Engineering*, 193:1323–1366, 2004.

[13] V. Gravemeier, S. Lenz, and W.A. Wall. Variational multiscale methods for incompressible flows. *International Journal of Computing Science and Mathematics*, 1(2–4):444–466, 2007.

[14] C. Förster, W.A. Wall, and E. Ramm. Stabilised finite element formulation for incompressible flow on distorted meshes. *Preprint*, 2007.

[15] M. Bischoff and E. Ramm. Shear deformable shell elements for large strains and rotations. *International Journal for Numerical Methods in Engineering*, 1997.

[16] M. Bischoff, W.A. Wall, K.-U. Bletzinger, and E. Ramm. Models and finite elements for thin-walled structures. In E. Stein, R. de Borst, and T.J.R. Hughes, editors, *Encyclopedia of Computational Mechanics - Volume 2: Solids, Structures and Coupled Problems*. John Wiley & Sons, 2004.

[17] W. Wall and T. Rabczuk. Fluid-structure interaction in lower airways of ct-based lung geometries. *International Journal for Numerical Methods in Fluids*, DOI:10.1002/fld.1763, 2008.

[18] J. DiRocco, D. Carney, and G. Nieman. The mechanism of ventilator-induced lung injury: Role of dynamic alveolar mechanics. In *Yearbook of Intensive Care and Emergency Medicine*. 2005.

[19] L. Wiechert, T. Rabczuk, M. Gee, R. Metzke, and W. A. Wall. Coupled problems in computational modeling of the respiratory system. In M. Resch et al., editor, *High Performance Computing on Vector Systems 2007*, pages 145–166. Springer, 2007.

[20] H. Kitaoka, S. Tamura, and R. Takaki. A three-dimensional model of the human pulmonary acinus. *Journal of Applied Physiology*, 88(6):2260–2268, Jun 2000.

[21] L. Wiechert and W.A. Wall. An artificial morphology for the mammalian pulmonary acinus. 2008, in preparation.

[22] H. Yuan, E. P. Ingenito, and B. Suki. Dynamic properties of lung parenchyma: mechanical contributions of fiber network and interstitial cells. *Journal of Applied Physiology*, 83(5):1420–31; discussion 1418–9, Nov 1997.

[23] G. A. Holzapfel, T. C. Gasser, and R. W. Ogden. Comparison of a multi-layer structural model for arterial walls with a fung-type model, and issues of material stability. *Journal of Biomechanical Engineering*, 126(2):264–275, Apr 2004.

[24] D. Balzani, P. Neff, J. Schröder, and G. A. Holzapfel. A polyconvex framework for soft biological tissues. Adjustment to experimental data. *International Journal of Solids and Structures*, 43(20):6052–6070, 2006.

[25] T. C. Gasser, R. W. Ogden, and G. A. Holzapfel. Hyperelastic modelling of arterial layers with distributed collagen fibre orientations. *Journal of the Royal Society Interface*, 3(6):15–35, 2006.

[26] Y. C. B. Fung. Elasticity of Soft Biological Tissues in Simple Elongation. *American Journal of Physiology*, 213:1532–1544, 1967.

[27] T. Sugihara, C. J. Martin, and J. Hildebrandt. Length-tension properties of alveolar wall in man. *Journal of Applied Physiology*, 30(6):874–878, Jun 1971.

[28] F. G. Hoppin Jr, G. C. Lee, and S. V. Dawson. Properties of lung parenchyma in distortion. *Journal of Applied Physiology*, 39(5):742–751, November 1975.

[29] R. A. Jamal, P. J. Roughley, and M. S. Ludwig. Effect of Glycosaminoglycan Degradation on Lung Tissue Viscoelasticity. *American Journal of Physiology - Lung Cellular and Molecular Physiology*, 280:L306–L315, 2001.

[30] S. A. F. Cavalcante, S. Ito, K. Brewer, H. Sakai, A. M. Alencar, M. P. Almeida, J. S. Andrade, A. Majumdar, E. P. Ingenito, and B. Suki. Mechanical Interactions between Collagen and Proteoglycans: Implications for the Stability of Lung Tissue. *Journal of Applied Physiology*, 98:672–9, 2005.

[31] R. Kowe, R. C. Schroter, F. L. Matthews, and D. Hitchings. Analysis of elastic and surface tension effects in the lung alveolus using finite element methods. *Jounal of Biomechanics*, 19(7):541–549, 1986.

[32] D. R. Otis, E. P. Ingenito, R. D. Kamm, and M. Johnson. Dynamic surface tension of surfactant TA: experiments and theory. *Journal of Applied Physiology*, 77(6):2681–2688, Dec 1994.

[33] M. Kojic, I. Vlastelica, B. Stojanovic, V. Rankovic, and A. Tsuda. Stress integration procedures for a biaxial isotropic material model of biological membranes and for hysteretic models of muscle fibres and surfactant. *International Journal for Numerical Methods in Engineering*, 68(8):893–909, 2006.

[34] J.E. Morris. Characterization of the dynamic behavior of lung surfactant and its components. *Master thesis (MIT)*, 1998.

[35] E. P. Ingenito, L. Mark, J. Morris, F. F. Espinosa, R. D. Kamm, and M. Johnson. Biophysical characterization and modeling of lung surfactant components. *Journal of Applied Physiology*, 86(5):1702–1714, May 1999.

[36] M. Griese. Pulmonary surfactant in health and human lung diseases: state of the art. *Eur Respir J*, 13(6):1455–1476, Jun 1999.

[37] T.J. Gregory, W.J. Longmore, M.A. Moxley, J.A. Whitsett, C.A. Reed, A.A. Fowler, L.D. Hudson, R.J. Maunder, C. Crim, and T.M. Hyers. Surfactant chemical composition and biophysical activity in acute respiratory distress syndrome. *Journal of Clinical Investigation*, 88:1976–1981, 1991.

[38] S. Rausch, C. Martin, S. Uhlig, R. Metzke, and W.A. Wall. Mechanical testing and inverse analysis for developing a material model of lung parenchym. *16th Congress of the European Society of Biomechanics, Lucerne (Switzerland), July 6 - 9, 2008*, accepted.

[39] A. Comerford, C. Stahl, J. Guttmann, and W.A. Wall. Coupled 3d impedance model of the human lungs. *8th Congress on Computational Mechanics, Venice (Italy), June 30 - July 5, 2008*, accepted.

[40] L. Wiechert and W.A. Wall. Multi-scale analysis of coupled lung tissue dynamics. *8th Congress on Computational Mechanics, Venice (Italy), June 30 - July 5, 2008*, accepted.